AGU PUBLICATIONS

JGR

Journal of Geophysical Research: Atmospheres

RESEARCH ARTICLE

10.1002/2015JD023326

Key Points:
- Nabro had no significant effect on ice cloud properties, frequency, and altitude
- No significant volcanic aerosol-ice cloud radiative effect after Nabro
- Ice cloud properties depend at most weakly on sulfate droplet abundance and size

Correspondence to:
A. Meyer,
angela.meyer@env.ethz.ch

Citation:
Meyer, A., J.-P. Vernier, B. Luo, U. Lohmann, and T. Peter (2015), Did the 2011 Nabro eruption affect the optical properties of ice clouds?, *J. Geophys. Res. Atmos.*, *120*, 9500–9513, doi:10.1002/2015JD023326.

Received 2 MAR 2015
Accepted 12 AUG 2015
Accepted article online 18 AUG 2015
Published online 23 SEP 2015

Did the 2011 Nabro eruption affect the optical properties of ice clouds?

A. Meyer[1,2], J.-P. Vernier[3], B. Luo[1,2], U. Lohmann[1,2], and T. Peter[1,2]

[1]Institute for Atmospheric and Climate Science, ETH Zurich, Zurich, Switzerland, [2]Center for Climate Systems Modeling, ETH Zurich, Zurich, Switzerland, [3]Science Systems and Applications, Inc., Hampton, Virginia, USA

Abstract The eruption of the Eritrean Nabro Volcano in June 2011 was the largest eruption since Mount Pinatubo in June 1991. The Nabro volcano emitted 1–1.5 megaton of sulfur dioxide into the lower stratosphere which resulted in a significant rise in the stratospheric sulfate aerosol burden in the months following the eruption. We have analyzed backscatter and extinction from ice clouds, as measured by the Cloud-Aerosol Lidar and Infrared Pathfinder Satellite Observations (CALIPSO) satellite between June 2006 and May 2014, to assess if volcanic aerosol produced by the Nabro eruption had affected ice clouds. We found no significant modifications of either of ice cloud optical properties (i.e., total backscattering and extinction), occurrence frequencies, or residence altitudes on a global scale. Using the analyzed optical properties as indicators of posteruptive ice cloud radiative forcing modifications, we find that the eruption had no significant volcanic aerosol-ice cloud radiative effect. Our results suggest that the investigated optical properties of ice and cirrus clouds are at most weakly dependent on the sulfate droplet number density and size distribution.

1. Introduction

Cirrus clouds play an important role in the radiative budget of the Earth [*Liou*, 1986]. They are thought to have a positive cloud radiative effect [*Chen et al.*, 2000]: Their cloud tops are at cold temperatures, so they emit less infrared radiation than clouds at lower altitudes or the surface. Moreover, the greater the cirrus optical thickness, the more terrestrial infrared radiation is emitted back to the ground. On the other hand, thicker cirrus clouds will scatter more solar radiation back to space. This cooling effect is outweighed by the aforementioned warming effects at typical cirrus optical thicknesses and altitudes [*Corti and Peter*, 2009].

Cirrus clouds form when a sufficiently moist air parcel is lifted to altitudes at which freezing is possible. Uplifts can occur in synoptic weather systems, in convection, in the tropical tropopause region (cold trap), and over mountainous terrain, as outlined in *Sassen* [2002]. In the case of contrail cirrus, aircraft exhausts provide the water vapor that is necessary for ice crystals to form. Tropospheric ice crystals can form in cirrus clouds in the upper troposphere at temperatures below $T_{hom} \approx -40°C$. Liquid droplets can freeze homogeneously only below T_{hom}. At warmer temperatures, freezing is possible in mixed-phase clouds at intermediate altitudes only via formation of ice germs on the surfaces of insoluble aerosol particles in a process called heterogeneous nucleation [*Pruppacher and Klett*, 1997]. Deposition nucleation is a heterogeneous nucleation pathway that can take place at temperatures below T_{hom}. Depending on an air parcel's initial humidity, *Wiacek et al.* [2010] outlined possible histories of cirrus- and mixed-phase cloud-forming air parcels and the relevance of homogeneous and heterogeneous nucleation therein.

In the context of this work, we study both cirrus clouds (including cirrostratus, cirrocumulus, and convective anvil cirrus) and the iced tops of mixed-phase clouds, i.e., the upper regions of nimbostratus and cumulonimbus clouds at temperatures $T < -40°C$. The global annual mean occurrence of Nimbostratus (Ns) and Cumulonimbus (Cb) clouds are 5–9% over land and 5–11% over ocean, while Cirrus (Ci), Cirrostratus (Cs), and Cirrocumulus (Cc) have a global annual mean occurrence of 6–22% over land and 6–14% over ocean [*Raschke et al.*, 2005; *Eastman and Warren*, 2013]. Adopting mean values of 7% and 14% for Ns + Cb and Ci + Cs + Cc over land (and of 8% and 10% over ocean), the fraction of iced tops of mixed-phase clouds relative to all ice clouds is 33% over land and 44% over ocean.

We sample the CALIPSO cloud observations based on a temperature criterion. Homogeneous freezing of micrometer-sized droplets of pure water occurs at about −38°C [*Koop et al.*, 2000]. To account for freezing point depression effects caused by atmospheric background concentrations of sulfate ions, we take −40°C as our ice cloud detection threshold. To test the sensitivity of our results with respect to this criterion, we repeated the analysis with −50°C, −60°C, and −70°C thresholds.

Stratospheric sulfate aerosols may have the potential to modify the microphysical and radiative properties, occurrence frequencies, and altitudes of ice clouds [*Sassen*, 1992; *Jensen and Toon*, 1992; *Wang et al.*, 1995; *Song et al.*, 1996; *Kübbeler et al.*, 2012]. The objective of this study is to investigate whether sulfate aerosols from the 2011 eruption of the Nabro Volcano have affected the optical properties (i.e., the total backscatter and extinction) of ice clouds on a global scale.

The Nabro Volcano (13.37°N, 41.70°E) is located in the Afar Depression, part of the East African Rift located in the Eritrean-Somalian border region. The eruption started on 12 June 2011 at around 21 UTC [*Vernier et al.*, 2013] and lasted for about a month. As reported by *Theys et al.* [2013], about 4.5 megaton (Mt) of sulfur dioxide (SO_2) were released during this time period, of which an estimated 1 Mt reached the lowermost stratosphere (N. Theys, personal communication, 2014). *Robock* [2013] provides an estimate of 1.5 Mt for the stratospheric SO_2 input following the eruption. The plume was rich in SO_2 and water vapor and poor in ash if any [*Clarisse et al.*, 2012; *Theys et al.*, 2013; *Penning de Vries et al.*, 2014]. A large fraction of the total SO_2 release occurred during the first 15 h of the eruption with injection heights between 15 and 18 km [*Theys et al.*, 2013]. SO_2 was injected directly to or above the tropopause region during this initial eruption and on 16 June 2011 [*Fromm et al.*, 2014]. Parts of the initial plume were transported toward East Asia in the upper troposphere [*Sawamura et al.*, 2012; *Penning de Vries et al.*, 2014]. *Bourassa et al.* [2012, 2013] have claimed that the plume was advected into the lower stratosphere by deep convection linked to the Asian monsoon. *Vernier et al.* [2013] and *Fromm et al.* [2013, 2014] argued that the plume was injected directly into the stratosphere instead. *Clarisse et al.* [2014] confirmed that lower parts of the initial plume underwent uplift in the Asian monsoon circulation, while *Fairlie et al.* [2014] asserted that this uplift was not due to monsoon convection but can be explained by quasi-isentropic flow alone.

Following the Nabro eruption, the stratospheric aerosol load increased mainly over Asia in the first month following the onset of the eruption [*Bourassa et al.*, 2012]. Figure 1 shows the stratospheric aerosol-to-molecular backscatter ratio from the first half of June 2011 to the second half of December 2011 based on nighttime backscatter measurements of the CALIPSO satellite. A stratospheric aerosol plume formed within weeks after the eruption onset, with the peak zonal mean aerosol optical depth at about 20 to 25°N. The feature observed near 10–12 km altitude North of 45°N in June and the first half of July is likely the plume from the Grimsvötn eruption in May 2011. Figure 2 shows the stratospheric aerosol optical depth at 532 nm above 15 km from June 2006 to May 2014 based on CALIPSO observations. By mid-August 2011, the Nabro plume had spread over the entire Northern Hemisphere (NH; Figures 1 and 2), and by end 2011 most of the stratospheric aerosol from the Nabro eruption had returned to the troposphere by stratosphere-to-troposphere exchange of air and sedimentation.

The Nabro eruption was likely the largest eruption since Mount Pinatubo (16°N) in June 1991 in terms of its stratospheric SO_2 injection. During the Pinatubo eruption, about 18 $\pm$ 4 Mt of SO_2 [*Guo et al.*, 2004] and 5–6 km^3 dense-rock equivalent of volcanic ash [*Wiesner et al.*, 2003] were released into the lower stratosphere. The Pinatubo eruption induced stratospheric warming and tropospheric cooling responses [*McCormick et al.*, 1995]. *Free and Angell* [2002] have examined the effects of volcanic eruptions on the vertical temperature structure of the troposphere using radiosonde data. They showed for the tropics that a tropospheric cooling followed the Pinatubo eruption which was maximal in the middle to upper troposphere, while the El Chichón (17°N, April 1982) and Agung eruptions (8°S, March 1963) exhibited a smaller and vertically more evenly distributed tropospheric temperature response. How a volcanic eruption affects the properties and abundance of ice particles may depend on the upper tropospheric temperature response to the eruption. As some eruptions may potentially induce significant temperature responses, our results may not be generalizable to arbitrary volcanic eruptions.

2. Potential Effects of Volcanic Aerosols on Ice Clouds

Sassen [1992] and *Sassen et al.* [1995] have reported cirrus clouds with ice crystal number densities as high as 600 per liter that were observed over Kansas in December 1991 with a ground-based lidar in the aftermath of the June 1991 eruption of Mount Pinatubo. They also suggested that the upper parts of two observed cirrus clouds, which were at temperatures between −40° and −50°C, i.e., below the homogeneous freezing

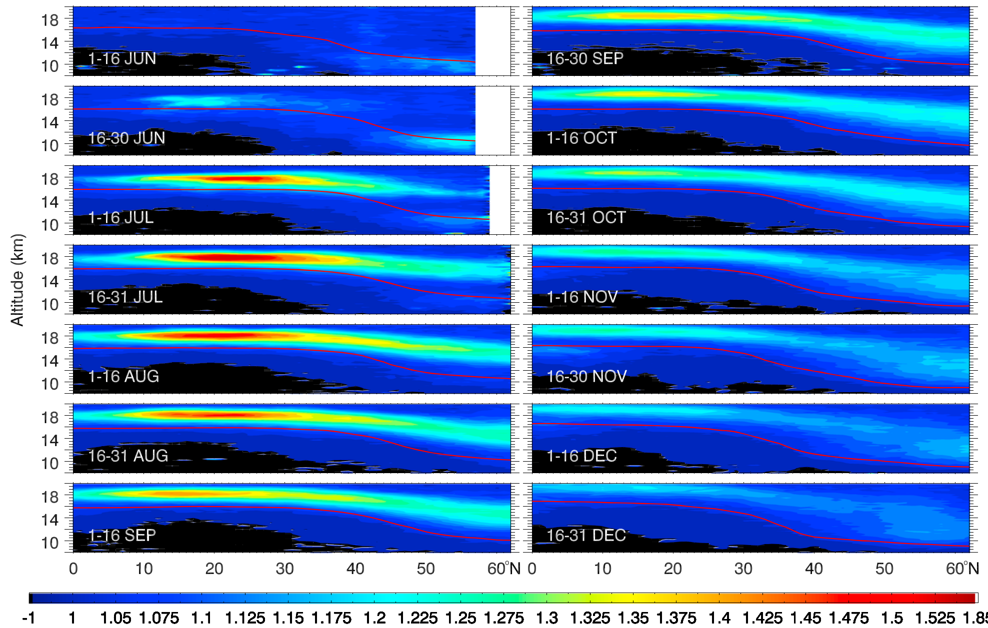

Figure 1. Zonal mean backscatter ratio (aerosol to molecular) of the Nabro plume between 0–62°N and 8–20 km altitude from June to December 2011 from CALIOP level 1 nighttime data. The red curve shows the zonal mean tropopause altitude from GEOS-5 data.

temperature of water, consisted mainly of supercooled aqueous sulfuric acid droplets based on depolarization data. The authors explained this observation with a freezing point depression that occurred in cloud droplets after an influx of volcanic aerosols into the cirrus-forming region. In the context of their study, a freezing point depression is the process of reducing the freezing point of water by adding a solute, sulfuric acid to it. The authors concluded that their observations provided evidence of a so far unobserved volcanic aerosol cirrus cloud climate feedback mechanism. *Sassen* [1992] also suggested that an influx of sulfate droplets into the upper troposphere might increase the abundance of cirrus clouds, because stratospheric sulfuric acid solution droplets that enter a cirrus-forming air mass after a volcanic eruption are typically larger than in volcanically quiescent times. The freezing probability of solution droplets increases with the droplet volume according to classical nucleation theory and in accordance with numerous laboratory measurements [*Pruppacher and Klett*, 1997]. Larger droplets are, therefore, more likely to freeze. Moreover, the larger a solution droplet and its sulfuric acid concentration, the lower the relative humidity that is required for the droplet to be in thermodynamic equilibrium with the gas phase, as described by the Kelvin and Raoult terms in the Köhler equation [*Pruppacher and Klett*, 1997]. Thus, the authors further suggested that cirrus clouds might occur at lower relative humidities after a strong volcanic eruption. Finally, they proposed a posteruptive increase in the cirrus lifetimes, because a greater abundance of large sulfate droplets might cause more and smaller ice crystals to form which would sediment less rapidly.

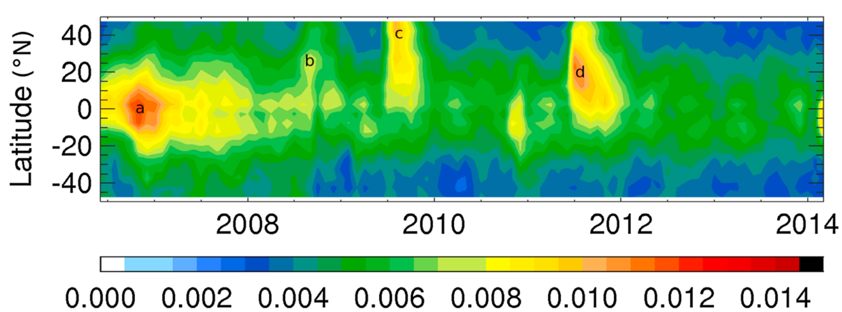

Figure 2. Zonal mean Aerosol Optical Depth at 532 nm above 15 km based on CALIPSO measurements (June 2006–May 2014), showing (a) Tavurvur, (b) Kasatochi, (c) Sarychev, and (d) Nabro eruption.

Wang et al. [1995] analyzed Stratospheric Aerosol and Gas Experiment (SAGE) II observations of subvisible tropical tropopause cirrus clouds following the El Chichón eruption in 1982. They found that clouds having high extinction coefficients become less frequent after the eruption, while clouds with low extinction coefficients become more frequent. The authors pointed out that, according to Mie theory, the cloud extinction coefficient decreases with increasing aerosol number densities if the effective cloud particle radii are below 0.8μm. They concluded that their cirrus cloud observations consist of particles of effective radii smaller than 0.8μm. They concluded further that the increase in number density of volcanic aerosol had induced this reduction in the cloud particle effective radii, because a greater number of solution droplets had been competing for the same amount of available water vapor after the eruption.

Song et al. [1996] analyzed outgoing longwave radiation data from the NOAA Climate Analysis Center and SAGE II and ground-based lidar observations. They found high-level cloudiness to increase with the global stratospheric aerosol load, particularly in the midlatitudes, and concluded that volcanic aerosol can significantly modify high-level cloudiness and thereby affect global climate. To explain their observations, the authors suggested that the posteruptive enhancement in solution droplet number densities increased the abundance of cloud condensation nuclei in the upper troposphere in posteruptive times, which may have enhanced upper level cloudiness.

Massie et al. [2003] examined Halogen Occultation Experiment and SAGE II observations of tropical tropopause cirrus. They found decreases in the occurrence frequency and the extinction of cirrus clouds after the 1991 eruption of Mount Pinatubo, in agreement with *Wang et al.* [1995]. The authors hypothesized that increases in ice nuclei number densities or changes in the strength or occurrence frequency of deep convective events might explain their observations. Moreover, they analyzed anomalies of radiosonde temperatures near the tropical tropopause together with SAGE II cirrus extinction measurements in order to investigate whether tropopause temperature changes as observed after the Pinatubo eruption can explain the posteruptive decrease in cirrus extinction. Based on their analysis, they excluded tropopause temperatures as a possible explanation of the observed posteruptive reduction in cirrus extinction.

Luo et al. [2002] analyzed three data sets that were derived from passive satellite instruments for evidence of large-scale modifications of cirrus cloud amounts or optical properties and found no such effects. They concluded that "previous studies showing some changes are probably isolated local effects." *Rolf et al.* [2012] examined ground-based lidar data of a cirrus cloud situated in a volcanic plume which originated from the 2010 eruption of the Icelandic Eyjafjallajökull Volcano. Running a microphysical box model along back trajectories, they concluded that the observed cirrus cloud must have formed by heterogeneous nucleation on the volcanic ash particles of the plume.

Turning to modeling studies, *Jensen and Toon* [1992] performed simulations on the effects of volcanic sulfate aerosols on cirrus clouds. They found that ice crystal number densities can increase by up to a factor of 5 when an air mass rich in sulfate droplets of stratospheric origin mixes with a tropospheric cirrus-forming air parcel. According to their estimates, this volcanic aerosol cirrus cloud effect may amount to a net surface warming of up to 8 W/m^2. The authors stressed the sensitivity of their results to a number of assumptions made and the need of further observational studies to constrain the model uncertainties. According to *Jensen et al.* [1994], the microphysical properties of cirrus clouds are, however, primarily sensitive to temperature and cooling rates of the cirrus-forming air mass and at most weakly related to the sulfate droplet number density.

Lohmann et al. [2003] simulated increases in ice crystal number density by about 50–100% in the tropical tropopause region following the Pinatubo eruption. They found that ice crystal number densities tended to be enhanced in regions where solution droplet number densities were low. Moreover, their results agreed with *Luo et al.* [2002] in that the sulfate aerosols of the simulated Pinatubo eruption have no significant cloud radiative effect.

Kübbeler et al. [2012] studied effects of stratospheric sulfate geoengineering on cirrus clouds and found that injections of 5 Mt SO_2/a caused reductions in ice crystal number densities by 5–50%. The simulated increase in stratospheric aerosol load warmed the upper troposphere and lower stratosphere (UTLS), because the aqueous sulfuric acid solution droplets absorb and re-emit terrestrial radiation and thereby warm the surrounding air masses. The UTLS warming in turn stabilized the middle and lower troposphere and thus reduced vertical wind velocities in cirrus-forming air parcels. This caused homogeneous ice nucleation rates to decline, resulting in cirrus clouds that were substantially thinner optically. The resulting radiative cooling effect made up

60% of the overall net radiative effect of the employed geoengineering scheme. *Cirisan et al.* [2013] studied stratospheric sulfate geoengineering effects on cirrus-forming air parcels in the northern midlatitudes from injections of 2–10 Mt SO_2/a. They found increased ice crystal number densities in cirrus clouds that formed in air masses strongly affected by stratospheric air and reduced ice crystal number densities in air masses only mildly affected by stratospheric air. The authors report a midlatitude cirrus radiative effect averaging out to less than 1% of the overall net radiative effect of their geoengineering scheme. Comparing to *Kübbeler et al.* [2012], the study of *Cirisan et al.* [2013] employs a more comprehensive microphysical scheme but focusses on the northern midlatitudes only and does not consider feedbacks, such as upper tropospheric temperature and humidity changes.

3. CALIPSO-Based Ice Cloud Statistics

Many passive satellite instruments are known to sample only the optically thick ice clouds and to miss optically thin ones [*Stubenrauch et al.*, 2013]. The CALIOP lidar on the CALIPSO satellite is able to detect even subvisible ice clouds. Based on the CALIOP backscatter and extinction signals, the residence altitudes, optical thicknesses, and occurrence frequencies of ice clouds can be calculated, which determine the cloud radiative effect [*Corti and Peter*, 2009]. Therefore, if significant modifications of the shape or position of the frequency distribution of lidar backscatter or extinction from clouds were observed in posteruptive seasons, this would suggest a cloud radiative effect of the volcanic aerosol. CALIOP is one of the most suitable instruments currently available for investigating the global radiative effect of volcanic aerosols on ice clouds. CALIPSO has been probing Earth's atmosphere nearly continuously since June 2006. It provides vertical profiles of backscatter and depolarization at 532 nm from particulates suspended in the troposphere and lower stratosphere during 15 orbits a day [*Winker et al.*, 2007, 2009]. The CALIPSO level 2 retrieval algorithms have been employed on the profiles to discriminate cloud and aerosol particles [*Vaughan et al.*, 2009]. We used the retrieved CALIPSO level 2 cloud profile product version 3 provisional (L2 CPro) [*Anselmo et al.*, 2007] to analyze nighttime measurements of particulate backscatter from 13 June 2006 to 31 May 2014. The data are provided at a resolution of 5–80 km along the ground track and 60 m vertically.

The 532 nm backscatter signal-to-noise ratios are worse during daytime because of the greater number of solar photons reaching the receiver telescope. Therefore, some thinner cirrus clouds may remain undetected by CALIPSO during daytime [*Winker et al.*, 2009]. Apparent daytime/nighttime differences in cirrus cloud occurrence frequency in the L2 CPro data product may result either from actual differences in occurrence frequency or from the poorer daytime signal-to-noise ratio. It is not possible to compare daytime and nighttime cirrus occurrence frequencies based on merely the L2 CPro data without being affected by the daytime low bias (M. Vaughan, personal communication, 2014). Therefore, our study focuses on the nighttime data only.

We also use atmospheric temperature data from the Goddard Earth Observing System Model data assimilation system, version 5 (GEOS-5) of NASA's Global Modeling and Assimilation Office. We filter the backscatter and extinction data based on the cloud-aerosol discrimination (CAD) score [*Liu et al.*, 2009, 2010] which provides a measure of the level of confidence in the result of the cloud-aerosol discrimination algorithm of *Vaughan et al.* [2009]. The CAD score distinguishes clouds from aerosol based on five-dimensional cloud and aerosol distributions, p_{cloud} and $p_{aerosol}$, that were developed based on four months of CALIOP observations and whose dimensions are the attenuated backscatter at 532 nm, the ratio of attenuated backscatter at 532 nm and at 1064 nm, the depolarization ratio, latitude, and altitude. The CAD score is defined as

$$\frac{p_{cloud} - p_{aerosol}}{p_{cloud} + p_{aerosol}} * 100 \tag{1}$$

where p_{cloud} and $p_{aerosol}$ take values in the range of 0 to 1. The CAD score values range from 0 to 100 for clouds and from 0 to −100 for aerosol. If there is no overlap between the 5-D cloud and aerosol distributions, clouds and aerosol can be distinguished from each other on the highest confidence level (CAD score = 100 for clouds, CAD score = −100 for aerosol). Absolute CAD score values larger than 70, between 50 and 70, between 20 and 50, and smaller than 20 correspond to high/ medium/ low/ no confidence in the cloud-aerosol discrimination according to Atmospheric Sciences Data Center (ASDC).

We filter the backscatter and extinction measurements such that any measurements with CAD score below 100 are discarded from our analysis. While (even at CAD score = 100) the CAD algorithm may not work fully reliably when discriminating mineral dust, volcanic ash, or smoke from cirrus clouds (ASDC), it performs well in distinguishing cirrus clouds from sulfate plumes based on their depolarization characteristics:

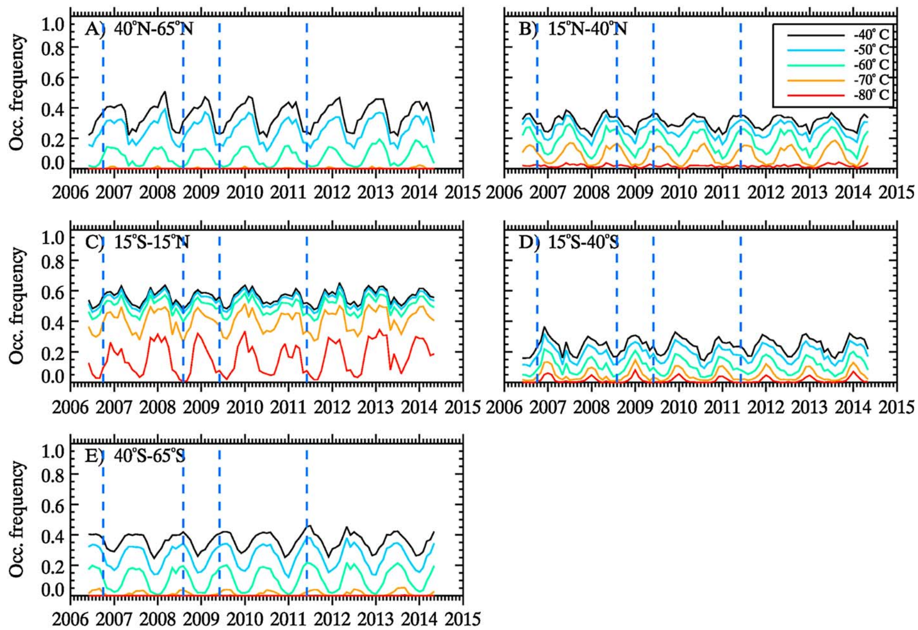

Figure 3. Monthly mean zonal mean nighttime ice occurrence frequencies based on 8 years of CALIPSO observations, from June 2006 to May 2014, for threshold temperatures of −40, −50, −60, −70, and −80°C. Tickmarks are in January. Dashed lines indicate (left to right) the eruptions of Tavurvur in October 2006, Kasatochi in August 2008, Sarychev in June 2009, and Nabro (13°N) in June 2011.

sulfate droplets have a depolarization ratio of close to zero because of their sphericity, whereas ice crystals in clouds at T≤−40°C typically produce lidar depolarization ratios of about 0.35 ± 0.1 [*Sassen and Benson*, 2001]. The good performance of the CAD algorithm in the case of sulfate-versus-cirrus discrimination is illustrated by the CALIPSO browse images of the 2011 Nabro plume (e.g., CALIPSO browse Images, http://www-calipso.larc.nasa.gov/products/lidar/browse_ima_ges/_show_detail.php?s=production_v=V3-01&browse_date=2011-07-18&orbit_time=00-17-10&page=1&granule_name=CAL_LID_L1-ValStage1-V3-01.2011-07-18T00-17-10ZN.hdf). The plume was rich in SO_2 but contained very little if any ash [*Clarisse et al.*, 2012; *Theys et al.*, 2013; *Penning de Vries et al.*, 2014]. Based on CALIPSO browse image inspections of the Nabro plume and on the negligible role of ash in the plume, we concluded that our results are not affected by a significant number of instances of volcanic aerosol misclassification as cloud.

Polar stratospheric clouds (PSC) are generally not contained in the L2 CPro data set [*Atmospheric Science Data Center*, 2013]. In some cases, we found the PSC removal incomplete though, so we screened the remaining PSC pixels by removing all backscatter measurements taken at altitudes above 14 km at latitudes polewards of 65°.

4. Results

As shown in Figure 1, a large fraction of the stratospheric aerosol that formed following the Nabro eruption returned to the northern hemispheric troposphere by the end of 2011. Posteruptive modifications of ice cloud properties would, therefore, mostly be expected in the Northern Hemisphere (NH) and within the first half year after the eruption.

4.1. Zonal Mean Ice Cloud Occurrence Frequencies

Figure 3 shows monthly mean zonal mean nighttime ice occurrence frequencies from the start of the operation period of the CALIPSO satellite in June 2006 to May 2014 for several latitude bands. In each panel, the black curve represents ice occurrence frequencies below a threshold temperature of −40°C, i.e., the ratio of the number of profiles which contain at least one in-cloud measurement below −40°C to the total number of profiles. One might expect that an influx of stratospheric sulfate aerosol into the troposphere may have the strongest impact on the cold and thin cirrus clouds of the uppermost troposphere. Thus, we also provide ice cloud occurrence frequencies for threshold temperatures of −50°C to −80°C, as indicated by the colored curves.

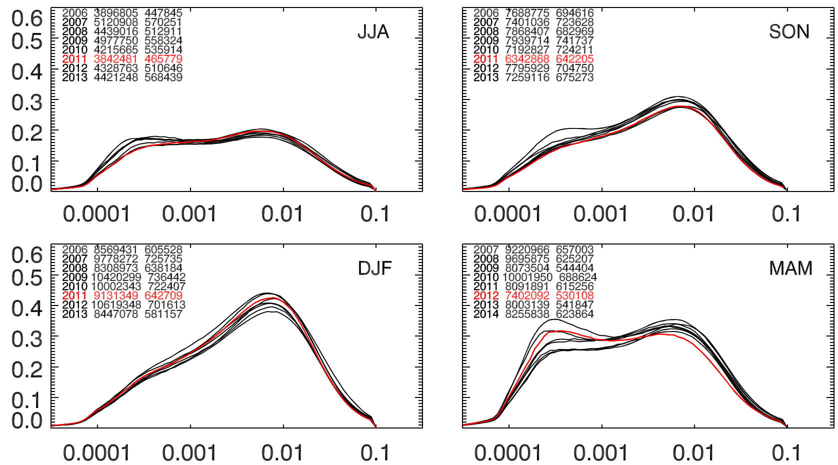

Figure 4. Backscatter distributions of CALIPSO nighttime ice observations over the northern midlatitudes 40–65°N (including land and ocean areas). The red curves are the backscatter distributions of the four seasons following the June 2011 Nabro eruption (JJA 2011 to MAM 2012). The black curves indicate the remaining seasons. All distributions have logarithmic bin widths of 0.05, i.e., 20 bins per magnitude. In each subpanel, each row pertains to one of the backscatter distributions, e.g., the row starting with "2011" in the DJF panel pertains to the red curve. The left column states the year, while the middle column shows the number of nighttime in-cloud backscatter measurements between 40 and 65°N and below −40°C that went into the distribution of the respective season and year. The right column provides the total number of nighttime CALIPSO profiles available between 40 and 65°N for the respective season and year; this includes profiles which contain clouds and profiles without any clouds (clear sky). For example, if for DJF 2011 there were only 2 orbits, each of which had 550 profiles between 40 and 65°N that contained 1800 backscatter measurements from clouds below −40°C at CAD = 100, the DJF 2011 row would read "2011 3600 1100," and the DJF 2011 distribution (red curve) would contain only 3600 data points.

In accordance with *Sassen et al.* [2008], we find that the ice occurrence frequencies exhibit a strong seasonal cycle in all latitude bands. Highest ice abundances are observed in the Intertropical Convergence Zone (ITCZ), where most convective activity and related transport of water vapor into the upper troposphere occurs. The tropical mean ice occurrence frequency exhibits a double-peaked shape with maxima in spring and autumn in accordance with the ITCZ equator-crossing times. It also has a weak El Niño signature superimposed: The 2009/2010 El Niño event shows up as a pronounced 2009 autumn peak that is right shifted by a few months toward wintertime. In the midlatitudes, ice is most frequently observed in the respective winter season.

The rightmost dashed line shows the Nabro eruption in June 2011. Also indicated are three other volcanic eruptions with stratospheric SO_2 input (see also Figure 2). None of the eruptions are followed by abnormally high or low ice occurrence frequencies in any of the five latitude bands. Even thin tropopause cirrus clouds which make up a substantial fraction of the −70°C and −80°C ice occurrence time series do not show a volcanic signature.

4.2. Ice Cloud Backscatter Distributions

Figure 4 shows frequency distributions of backscatter measurements of nighttime ice cloud observations taken over the northern midlatitude land and ocean areas (40–65°N) for different seasons based on the CALIPSO L2 CPro data set. The backscatter measurements shown are the total (perpendicular + parallel) lidar backscatter at 532 nm after attenuation correction. They are provided in the CALIPSO level 2 cloud profile product version 3 provisional (L2 CPro) [*Anselmo et al.*, 2007]. The red curves represent frequency distributions of the four seasons following the Nabro eruption, i.e., June, July, and August (JJA) 2011, September, October, and November (SON) 2011, December, January, and February (DJF) 2011/2012, and March, April, and May (MAM) 2012. Seasons of the other years are plotted in black.

The histograms contain only positive backscatter values, even though about 2% of the L2 CPro ice crystal backscatter values are negative. Negative values mostly occur when the corresponding attenuated backscatter values are negative as well, which can be the case in weakly scattering parts of clouds (M. Vaughan, personal communication, 2014). We have omitted the negative backscatter values in the logarithmic histograms but counted them in the occurrence frequency plots.

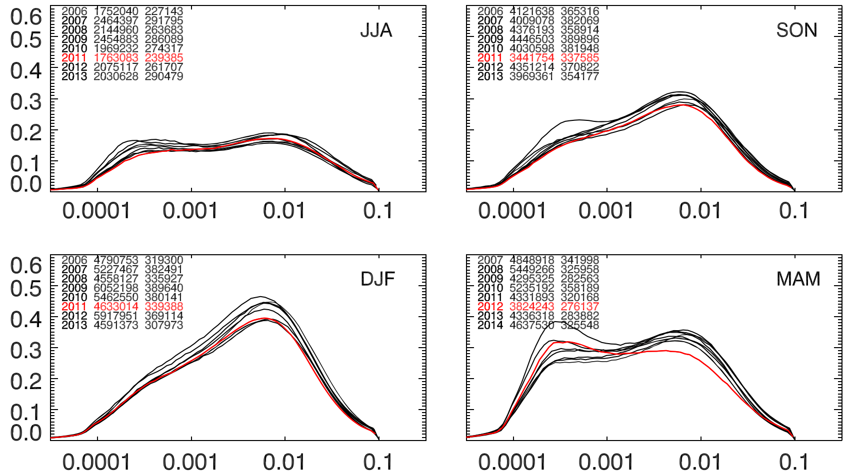

Figure 5. As Figure 4 but for northern midlatitudes land areas.

There are months, like May 2013, for which much fewer CALIPSO measurements are available than for others, e.g., due to orbit maintenance. In order to account for this circumstance, we have normalized each histogram by the number of profiles that were sampled to construct it. Thus, a hypothetical doubling in ice occurrence frequency would show as a doubling in height of the corresponding backscatter histogram, because ice would occur twice as often in each profile. So a backscatter histogram shifted upwards (downwards) by a significant amount would indicate an increase (decrease) in the ice occurrence frequency. On the other hand, a significant left or right shift of a particular histogram would hint at the occurrence of larger ice crystals or higher ice crystal number densities. We normalized by the number of profiles, rather than by, e.g., the number of measurements below −40°C, because the latter would include stratospheric measurements. Since background tropospheric aerosol composition and number densities generally differ over land and oceans, we provide backscatter distributions for NH midlatitude land and ocean areas separately in Figures 5 and 6.

As shown in Figures 4–6, there is significant interannual variability in the heights of the distributions, i.e., in the number of ice crystal backscatter measurements per backscatter range per profile, in all seasons. The variability is most pronounced in DJF and MAM which is likely induced by the year-to-year variability of midlatitude cyclone frequency and location. The backscatter distributions do not exhibit any systematic upward/downward or left/right shifts in the posteruptive seasons (JJA, SON, DJF 2011, and MAM 2012) following the 12 June 2011 eruption. The posteruptive backscatter distributions (red curves) do not stand out from among other years, except in DJF 2011 over NH midlatitude oceans and in MAM 2012 over the NH midlatitude land areas. Over NH midlatitude oceans, the DJF distributions with the second and third highest peaks

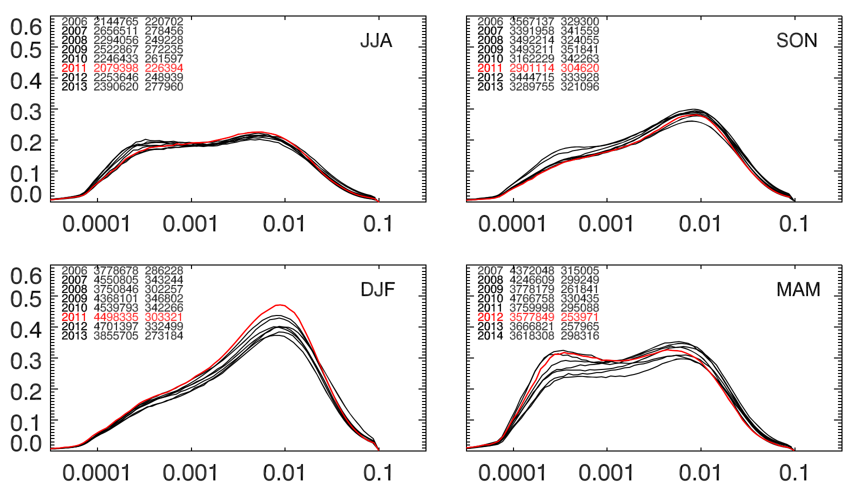

Figure 6. As Figure 4 but for orthern midlatitudes ocean areas.

pertain to volcanically quiescent periods (DJF 2012 and 2013). Given the substantial interannual variability, only the MAM 2012 backscatter distribution might possibly constitute a significant deviation from the interannual mean. For each of the backscatter bins, we have calculated the mean and standard deviation based on MAM of years 2007–2011, 2013, and 2014. We found that the MAM 2012 backscatter values in the range of 0.0034 and 0.0169 km^{-1} sr^{-1} (or equivalently $10^{-2.47}$ and $10^{-1.77}$ km^{-1} sr^{-1}) lie below the 7 year mean by three standard deviations (99.7% confidence level). In the same manner, we performed a statistical test for DJF 2011, in which we found that the DJF 2011 backscatter values do not lie outside of three standard deviations from the mean, except for one single backscatter bin (the one centered at $10^{-2.0032}$ km^{-1} sr^{-1} = 0.0099 km^{-1} sr^{-1}) which is just about significant at the 3 sigma level.

However, to make a clear statement about the significance of the DJF 2011 and, in particular, the MAM 2012 backscatter anomalies, we would require measurement time series much longer than 8 years in order to allow for a better estimate of the mean and standard deviation of the backscatter per profile in each backscatter range and to test the assumption of normality distribution. Moreover, we would need the deviation to show up also in the posteruptive seasons of JJA 2011 and, in particular, SON 2011, as the strongest potential impact of volcanic aerosol on ice clouds is expected in the first 6 months after the Nabro eruption. By MAM 2012, i.e., 8.5 to 10.5 months after the eruption, the stratospheric aerosol burden has decayed approximately to pre-Nabro values, as can be seen in Figure 2.

Other than these, there are no potentially significant deviations in posteruptive seasons, even at lower threshold temperatures of −50 and −60°C (not shown), i.e., even in ice clouds at greater altitudes. We have also evaluated the ice cloud backscatter distributions at lower latitudes, namely, for the latitude bands 15°N–40°N and 15°S–15°N (over land, oceans, and both) and have found no significant posteruptive deviations for these lower latitude bands either. We also examined the distributions of the extinction of the CALIOP beam at 532 nm in clouds at temperatures below −40°C at 40°N–65°N, 15°N–40°N, and 15°S–15°N (again over land, oceans, and both) and found no further significant posteruptive deviations in addition to the ones reported above.

The backscatter distributions of Figures 4–6 consistently show a first mode that peaks at about $7 \cdot 10^{-3}$ km^{-1} sr^{-1}. A second mode is present which peaks at about $3 \cdot 10^{-4}$ km^{-1} sr^{-1} and is particularly pronounced in springtime and in summer. Comparing our backscatter distributions to distributions of ice crystal extinction derived from simulations of the global aerosol-climate model ECHAM-HAM [*Zhang et al.*, 2012], we found that no second mode is present in the simulated ice clouds, which lead us to examine whether the observed second mode actually stems from ice crystal backscatter. We noted that the seasonality of the second backscatter mode matches well with the seasonality of upper tropospheric aerosol extinction that is present in particular in springtime but also in summer at NH midlatitudes in the SAGE II extinction data set. *Thomason and Vernier* [2013] reported a similar seasonality in aerosol extinction in the SAGE II data. Springtime is a major mineral dust emission time, and a substantial fraction of the uplifted dust is transported to the upper troposphere [*Wiacek et al.*, 2010]. Mineral dust aerosol and thin ice clouds have similar backscatter and depolarization characteristics, which is why the CALIPSO cloud-aerosol discrimination algorithm does not work fully reliably on dust aerosol plumes [e.g., *Chen et al.*, 2010]. Thus, the second (low-backscatter) mode in the distributions of Figures 4–6 is likely caused by the presence of aerosol particles misclassified as clouds by the level 2 cloud-aerosol discrimination algorithm.

The low-backscatter mode is also evident in the two-dimensional histograms of Figure 7 which are normalized frequency distributions of backscatter and residence temperature of ice cloud measurements made between 45–60°N for the posteruptive seasons (top row) and the 8 year mean (bottom row) as filled contours. The low-backscatter mode of Figure 7 indicates that the particles that cause the scattering reside at temperatures of about −50°C. Figure 8a shows the zonal mean aerosol scattering ratio (relative to molecular backscatter) for altitudes of 8–22 km over 30–60°N based on CALIPSO level 1 measurements after cloud clearing. The seasonality of the aerosol plume in the upper troposphere is evident. The plume is strongest in late spring/early summer. Its residence altitude of about 9–11 km is consistent with the typical residence temperature of about −53°C (Figure 7). Figure 8b shows the zonal mean aerosol scattering ratio over 0–30°N for comparison.

The prominent second mode in SON of Figure 5, peaking at about $6 \cdot 10^{-4}$ km^{-1} sr^{-1}, corresponds to the backscatter distribution of fall 2008. The Kasatochi volcano erupted in the Aleutian Island chain at 52°N, 175°W on 8 August 2008. Besides some volcanic ash, its plume contained mostly sulfate aerosol and resided in the

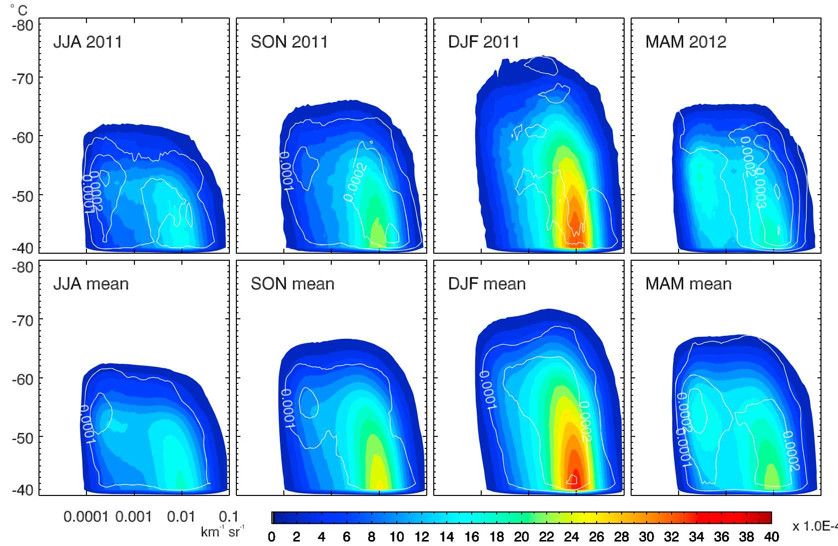

Figure 7. Histograms of CALIPSO nighttime backscatter measurements and corresponding temperatures from the GEOS-5 model for 45–60°N for the posteruptive seasons JJA 2011 to MAM 2012 (top row) and 8 year seasonal means (bottom row). To allow intercomparison between histograms, each one is normalized by the number of profiles that contributed to it. The contour lines (in white) have been smoothed by a nearest neighbor running average to improve readability. They are linearly increasing in steps of 0.0001.

UTLS of the NH middle and high latitudes until November 2008 [*Hoffmann et al.*, 2010; *Wang et al.*, 2013]. It cannot be ruled out that the Kasatochi aerosols have induced the nucleation of ice crystals. However, a substantial part of the peak is likely caused by parts of the plume being misclassified as cirrus cloud by the CALIPSO cloud retrieval algorithms. Visual inspection of vertical feature mask browse images in September and October 2008 supports the latter.

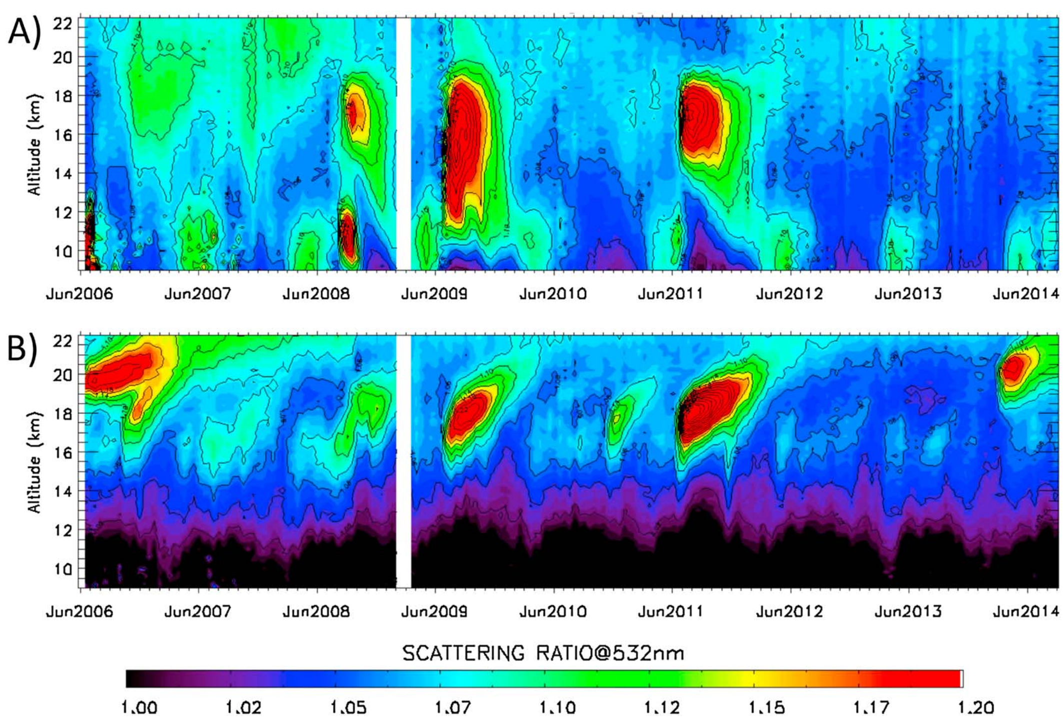

Figure 8. Zonal mean scattering ratio (aerosol to molecular) based on CALIOP observations (a) over 30–60°N and (b) over 0–30°N (panel B).

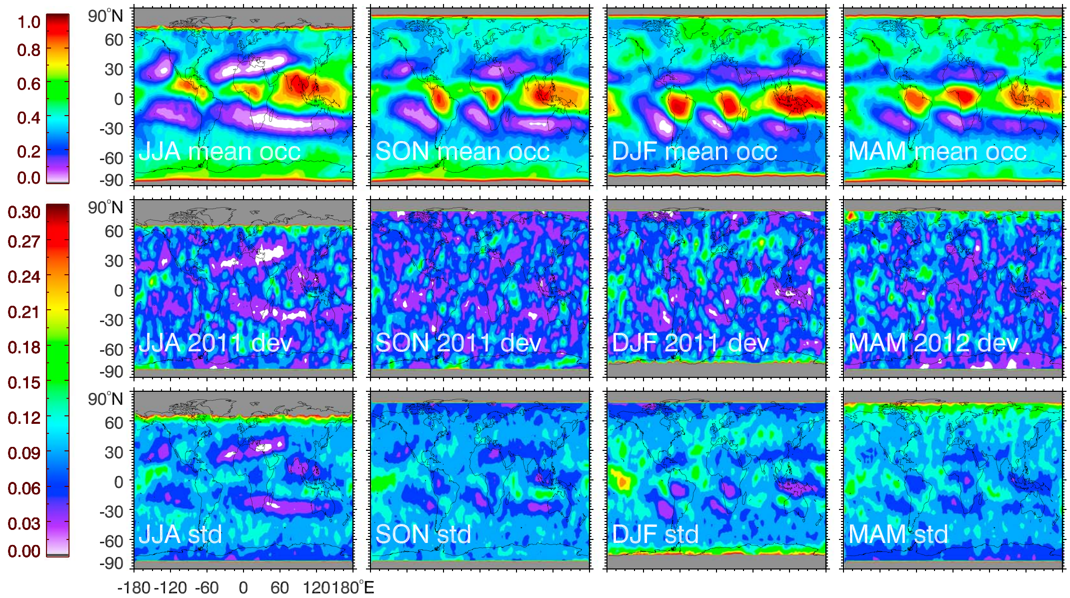

Figure 9. Interannual variability of seasonal nighttime ice occurrence frequencies. (top row) Mean seasonal ice cloud occurrence frequencies from 8 years of CALIPSO observations. (middle row) Absolute values of deviations from the 8 year seasonal means (shown in Figure 9 (upper row)) of the posteruptive seasons JJA 2011 to MAM 2012. (bottom row) Seasonal standard deviation calculated from 8 years of CALIPSO observations. Regions without data are shaded in gray. The upper colorbar refers to Figure 9 (top row) and the lower colorbar to Figure 9 (middle and bottom rows).

4.3. Interannual Variability of Seasonal Ice Cloud Occurrence and Altitudes

The frequency distributions of Figure 7 are histograms of logarithmic bin width 0.05 for backscatter and of 1°C bin width for temperature. Each histogram bin provides the number of nighttime backscatter measurements in the indicated backscatter and temperature ranges, normalized by the number of profiles that contributed to the histogram. As indicated in the figure, for NH midlatitude ice clouds, temperature-backscatter combinations of between −40 and −50°C and about 10^{-2} km^{-1} sr^{-1} (corresponding to an extinction of about 0.2 km^{-1}) are most frequent. The posteruptive distributions are very similar to the 8 year means. The contour lines indicate the interannual variability (standard deviation) present in the backscatter-temperature distribution entries (bottom row) and the posteruptive deviation from the mean (top row). None of the posteruptive backscatter-temperature bins lies outside of three standard deviations of the 8 year mean, so there is no indication of a significant posteruptive modification of ice cloud residence altitudes in the NH midlatitudes.

Figure 9 compares the posteruptive deviations in ice occurrence frequencies with the amount of interannual variability in ice occurrence on a 3° × 3° grid. The threshold temperature used was −40°C. As indicated by the standard deviations in the bottom row, the interannual variability is highest over the tropical pacific in SON and DJF, which is a signature of the El Niño-Southern oscillation, and lowest in subtropical regions with low ice cloud occurrence, such as the summertime Southern Hemisphere subtropical Indian Ocean. The deviations of the posteruptive seasons (as shown in the middle row) from the 8 year mean (top row) have been smoothed by a nearest neighbor running mean to improve the readability. For each season, the posteruptive deviations in ice cloud occurrence generally fall within one standard deviation of the 8 year mean. None of the posteruptive deviations fall outside of three standard deviations from the 8 year mean in any season.

There may be instances when CALIOP measurements of clouds, in particular of thin cirrus clouds, can be misclassified as aerosol by the CALIPSO level 2 CAD algorithm. To investigate whether our results are affected in this manner, we have studied the backscatter and depolarization distributions of the CALIOP measurements that were classified as "aerosol" in the CALIPSO level 2 aerosol profile product version 3 provisional (L2 APro). All CALIOP signal returns other than from "clear air" or from the surface are classified as either "aerosol" or "cloud" by the CAD algorithm. Aerosol measurements are provided in the L2 APro product, while cloud measurements are in the L2 CPro product. Therefore, if significant amounts of thin cirrus clouds were misclassified in a posteruptive season, this would show up in the aerosol backscatter-depolarization histograms of that season. Figure 10 shows backscatter-depolarization distributions of CALIOP nighttime

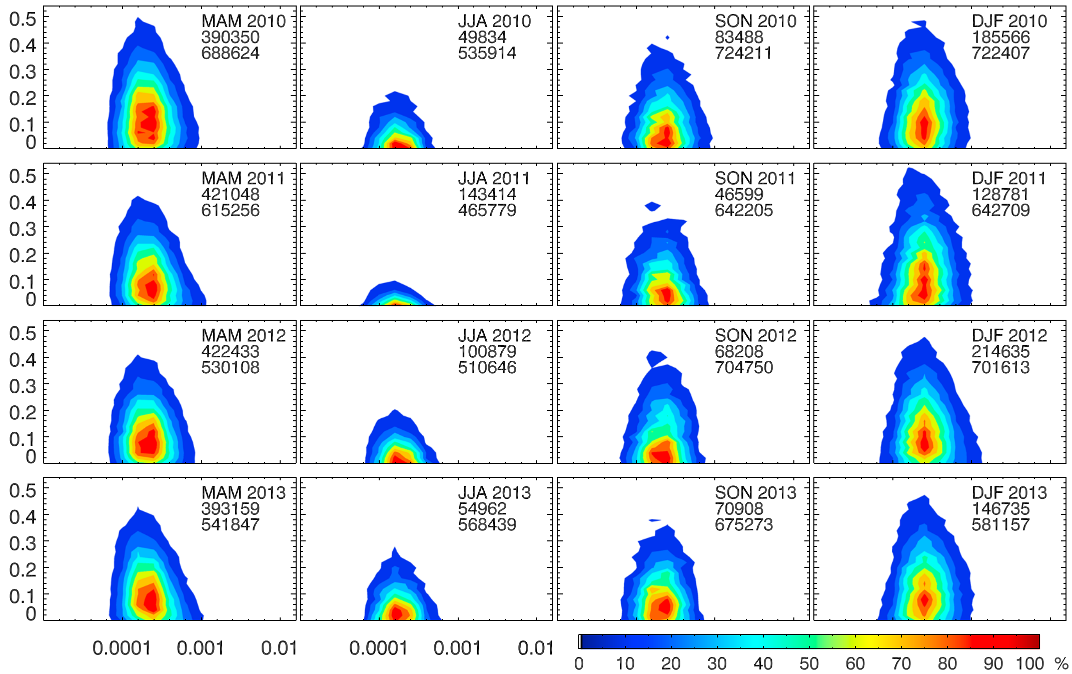

Figure 10. Seasonal distributions of aerosol backscatter and depolarization of CALIOP nighttime measurements taken between 40 and 65°N for years 2010–2013 at temperatures below −40°C and CAD scores between −70 and −100. The UTLS was largely volcanically unperturbed in all seasons of 2010–2013 except for the Nabro posteruptive period (JJA 2011 to MAM 2012). Each backscatter-depolarization histogram is normalized by the highest number of counts occurring in its bins: dark red histogram pixels correspond to 90–100% of the highest number of counts, while dark blue pixels correspond to 0–10% of that value. The numbers in the panels indicate season and year, the number of measurements (just below), and the number of profiles that contributed to the histogram.

aerosol measurements taken between 40 and 65°N for years 2010–2013 at temperatures below −40°C and CAD scores between −70 and −100 (i.e., high confidence in the classification as aerosol). We present this time period because the UTLS was largely volcanically unperturbed in all seasons of 2010–2013 except for the Nabro posteruptive period (JJA 2011 to MAM 2012), see Figure 2. In Figure 10, each backscatter-depolarization histogram is normalized by the highest number of counts occurring in its bins. Dark red histogram pixels correspond to 90–100% of the highest number of counts, while dark blue pixels correspond to 0–10% of that value. As in Figures 4–6, the numbers in the panels of Figure 10 indicate season and year, the number of measurements (just below), and the number of profiles that contributed to the histogram. Typical lidar depolarization ratios observed for thin cirrus clouds at temperatures below −40°C are 0.35 ± 0.1 [*Sassen and Benson*, 2001] and typical backscatter values are below 10^{-3} km^{-1} sr^{-1}. Figure 10 shows no changes in the thin cirrus region thus defined in the posteruptive seasons of JJA 2011 to MAM 2012 as compared to the corresponding volcanically quiescent seasons. Rather, JJA 2011 is somewhat shifted toward lower depolarisation ratios because comparatively large amounts of sulfate droplets from the Nabro eruption (which have depolarisation ratios well below 0.1) are detected in that season, so relatively more aerosol measurements at low depolarisation ratios were made in JJA 2011 than in JJAs of other years. In a similar manner, we have investigated the backscatter-depolarization distributions of 15–40°N and 15°S–15°N and have not found significant amounts of cirrus cloud measurements misclassified as aerosol in those latitude bands either. Moreover, we found no systematic misclassifications of thin cirrus clouds as aerosol in the CALIPSO browse images of the posteruptive seasons.

5. Conclusions

We have analyzed 8 years of CALIPSO backscatter and extinction data characterizing ice clouds and find that the June 2011 eruption of the Eritrean Nabro Volcano did not cause a statistically significant modification of the optical properties (total backscattering and extinction), occurrence frequencies, or residence altitudes of ice clouds on a global scale, even in the uppermost troposphere. We conclude that the eruption had no significant volcanic aerosol-ice cloud radiative effect in the four seasons following it.

According to classical homogeneous nucleation theory, the largest droplets of any sulfate aerosol population are the ones to freeze first [*Pruppacher and Klett*, 1997; *Kärcher and Lohmann*, 2002; *Cirisan et al.*, 2013]. Simulations of the Nabro sulfate plume performed with the global chemistry-climate model SOCOL-AER [*Sheng et al.*, 2015] indicate that the number densities of the largest sulfate aerosol droplets ($\approx$0.1μm) increased by a factor of 3–4 in the NH midlatitude tropopause region at the lower edge of the plume (and by more than a factor of 10 at higher altitudes) in the months following the Nabro eruption. These increases are consistent with measurements of aerosol number densities made over Laramie (41°N), Wyoming made on 1 June, 28 July, and 4 November 2011 (supporting online material of *Bourassa et al.* [2012]). In view of such a large increase in sulfate aerosol abundance in ice-forming air masses, our results suggest that the optical properties of ice and cirrus clouds are at most weakly dependent on the sulfate droplet number density and size. This is in agreement with the analysis of *Luo et al.* [2002] and with the simulations of *Jensen et al.* [1994] who found that temperature and cooling rates are the main determinants of ice crystal number density.

Our study does not exclude the possibility of local ice cloud modifications like those observed by *Sassen* [1992]. CALIPSO's inherent resolution is 30 m vertically and about 70 m horizontally, corresponding to the diameter of the lidar's ground footprint. The L2 CPro data employed in this study are provided at a resolution of 60 m vertically and 5–80 km horizontally. In order to avoid sampling artifacts and reduce interannual variability, we have evaluated the L2 CPro data on coarse 3°×3° grids or as zonal means. While ice cloud modifications on scales below this resolution cannot be excluded, they would have been locally limited effects.

Acknowledgments
We thank David Neubauer for providing ECHAM-HAM ice crystal backscatter histograms and Jianxiong Sheng and Andrea Stehnke for providing SOCOL-AER simulated Nabro sulfate aerosol size distributions. We also thank three anonymous reviewers for their constructive suggestions and comments. We also acknowledge helpful discussions with Mark Vaughan, Heini Wernli, and Marc von Hobe. The CALIPSO data were provided by the Atmospheric Science Data Center at NASA Langley Research Center. They are publicly available from https://eosweb.larc.nasa.gov/. This work was supported by ETH Research grant CH2-01 11-1.

References

Anselmo, T., et al. (2007), CALIPSO data management system. Data products catalog, release 2.4, *NASA Doc., PC-SCI-503*, NASA Langley Research Center, Hampton, Va. [Available at http://www-calipso.larc.nasa.gov/products/CALIPSO_DPC_Rev2x4.pdf.]

Atmospheric Science Data Center (2013), CALIPSO Quality Statements, NASA Langley Research Center, Hampton, Va. [Available at https://eosweb.larc.nasa.gov/sites/default/files/project/calipso/quality_summaries/CALIOP_L2VFMProducts_3.01.pdf, 2 June 2015].

Bourassa, A., et al. (2012), Large volcanic aerosol load in the stratosphere linked to Asian monsoon transport, *Science*, *337*, 78–81, doi:10.1126/science.1219371.

Bourassa, A., et al. (2013), Response to comments on "Large volcanic aerosol load in the stratosphere linked to Asian monsoon transport", *Science*, *339*(6120), 647, doi:10.1126/science.1227961.

Chen, B., et al. (2010), Detection of dust aerosol by combining CALIPSO active lidar and passive IIR measurements, *Atmos. Chem. Phys.*, *10*, 4241–4251, doi:10.5194/acp-10-4241-2010.

Chen, T., et al. (2000), Radiative effects of cloud-type variations, *J. Clim.*, *13*, 264–286, doi:10.1175/1520-0442(2000)013<0264:REOCTV>2.0.CO;2.

Cirisan, A., P. Spichtinger, B. P. Luo, D. K. Weisenstein, H. Wernli, U. Lohmann, and T. Peter (2013), Microphysical and radiative changes in cirrus clouds by geoengineering the stratosphere, *J. Geophys. Res. Atmos.*, *118*, 4533–4548, doi:10.1002/jgrd.50388.

Clarisse, L., D. Hurtmans, C. Clerbaux, J. Hadji-Lazaro, Y. Ngadi, and P.-F. Coheur (2012), Retrieval of sulphur dioxide from the Infrared Atmospheric Sounding Interferometer (IASI), *Atmos. Meas. Tech.*, *5*, 581–594, doi:10.5194/amt-5-581-2012.

Clarisse, L., P.-F. Coheur, N. Theys, D. Hurtmans, and C. Clerbaux (2014), The 2011 Nabro eruption, a SO_2 plume height analysis using IASI measurements, *Atmos. Chem. Phys.*, *14*(6), 3095–3111, doi:10.5194/acp-14-3095-2014.

Corti, T., and T. Peter (2009), A simple model for cloud radiative forcing, *Atmos. Chem. Phys.*, *9*, 5751–5758.

Eastman, R., and S. G. Warren (2013), A 39-yr survey of cloud changes from land stations worldwide 1971-2009: Long-term trends, relation to aerosols, and expansion of the tropical belt, *J. Clim.*, *26*, 1286–1303, doi:10.1175/JCLI-D-12-00280.1.

Fairlie, T. D., J.-P. Vernier, M. Natarajan, and K. M. Bedka (2014), Dispersion of the Nabro volcanic plume and its relation to the Asian summer monsoon, *Atmos. Chem. Phys.*, *14*(13), 7045–7057, doi:10.5194/acp-14-7045-2014.

Free, M., and J. K. Angell (2002), Effect of volcanoes on the vertical temperature profile in radiosonde data, *J. Geophys. Res.*, *107*(D10), ACL 16–1–ACL 16-10, doi:10.1029/2001JD001128.

Fromm, M., G. Nedoluha, and Z. Charvát (2013), Comment on "Large volcanic aerosol load in the stratosphere linked to Asian monsoon transport", *Science*, *339*, 6120, doi:10.1126/science.1228605.

Fromm, M., G. Kablick III, G. Nedoluha, E. Carboni, R. Grainger, J. Campbell, and J. Lewis (2014), Correcting the record of volcanic stratospheric aerosol impact: Nabro and Sarychev Peak, *J. Geophys. Res. Atmos.*, *119*, 10,343–10,364, doi:10.1002/2014JD021507.

Guo, S., G. J. S. Bluth, W. I. Rose, I. M. Watson, and A. J. Prata (2004), Re-evaluation of SO_2 release of the 15 June 1991 Pinatubo eruption using ultraviolet and infrared satellite sensors, *Geochem. Geophys. Geosyst.*, *5*, Q04001, doi:10.1029/2003GC000654.

Hoffmann, A., C. Ritter, M. Stock, M. Maturilli, S. Eckhardt, A. Herber, and R. Neuber (2010), Lidar measurements of the Kasatochi aerosol plume in August and September 2008 in Ny-Ålesund, Spitsbergen, *J. Geophys. Res.*, *115*, D00L12, doi:10.1029/2009JD013039.

Jensen, E., and O. B. Toon (1992), The potential effects of volcanic aerosols on cirrus-clouds microphysics, *Geophys. Res. Lett.*, *19*, 1759–1762.

Jensen, E. J., O. B. Toon, D. L. Westphal, S. Kinne, and A. J. Heymsfield (1994), Microphysical modeling of cirrus: 2. Sensitivity studies, *J. Geophys. Res.*, *99*, 10,443–10,454, doi:10.1029/94JD00226.

Kärcher, B., and U. Lohmann (2002), A parameterization of cirrus cloud formation: Homogeneous freezing of supercooled aerosols, *J. Geophys. Res.*, *107*(D2), 4010, doi:10.1029/2001JD000470.

Koop, T., B. Luo, A. Tsias, and T. Peter (2000), Water activity as the determinant for homogeneous ice nucleation in aqueous solutions, *Nature*, *406*, 611–614, doi:10.1038/35020537.

Kübbeler, M., U. Lohmann, and J. Feichter (2012), Effects of stratospheric sulfate aerosol geo-engineering on cirrus clouds, *Geophys. Res. Lett.*, *39*, L23803, doi:10.1029/2012GL053797.

Liou, K. N. (1986), Influence of cirrus clouds on weather and climate: A global perspective, *Mon. Weather Rev.*, *114*, 1167–1199, doi:10.1175/1520-0493(1986)114<1167:IOCCOW>2.0.CO;2.

Liu, Z., et al. (2009), The CALIPSO lidar cloud and aerosol discrimination: Version 2 algorithm and initial assessment of performance, *J. Atmos. Oceanic Technol.*, *26*, 1198–1213, doi:10.1175/2009JTECHA1229.1.

Liu, Z., et al. (2010), The CALIPSO cloud and aerosol discrimination: Version 3 algorithm and test results, NASA Langley Research Center, Hampton, Va. [Retrieved from http://www-calipso.larc.nasa.gov/resources/pdfs/ILRC_LaRC_2010/Liu_ILRC25_2010.pdf, 2 June 2015.]

Lohmann, U., B. Kärcher, and C. Timmreck (2003), Impact of the Mount Pinatubo eruption on cirrus clouds formed by homogeneous freezing in the ECHAM4 GCM, *J. Geophys. Res.*, *108*(D18), 4568, doi:10.1029/2002JD003185.

Luo, Z., W. B. Rossow, T. Inoue, and C. J. Stubenrauch (2002), Did the eruption of the Mt. Pinatubo volcano affect cirrus properties?, *J. Clim.*, *15*, 2806–2820, doi:10.1175/1520-0442(2002)015<2806:DTEOTM>2.0.CO;2.

Massie, S., W. Randel, F. Wu, D. Baumgardner, and M. Hervig (2003), Halogen occultation experiment and stratospheric aerosol and gas experiment II observations of tropopause cirrus and aerosol during the 1990s, *J. Geophys. Res.*, *108*(D7), 4222, doi:10.1029/2002JD002662.

McCormick, M. P., L. W. Thomason, and C. R. Trepte (1995), Atmospheric effects of the Mt Pinatubo eruption, *Nature*, *373*, 399–404, doi:10.1038/373399a0.

NASA Langley Research Center's Atmospheric Science Data Center (2013), CALIPSO quality statements: Lidar level 2 cloud and aerosol profile products version releases: 3.01, 3.02, *Tech. Rep.*, NASA Langley Research Center, Hampton, Va.

Penning de Vries, M. J. M., S. Dörner, J. Pukite, C. Hörmann, M. D. Fromm, and T. Wagner (2014), Characterisation of a stratospheric sulfate plume from the Nabro volcano using a combination of passive satellite measurements in nadir and limb geometry, *Atmos. Chem. Phys.*, *14*(15), 8149–8163, doi:10.5194/acp-14-8149-2014.

Pruppacher, H. R., and J. D. Klett (1997), *Microphysics of Clouds and Precipitation*, 2nd ed., Kluwer Acad., Dordrecht, Netherlands.

Raschke, E., A. Ohmura, W. B. Rossow, B. E. Carlson, Y.-C. Zhang, C. Stubenrauch, M. Kottek, and M. Wild (2005), Cloud effects on the radiation budget based on ISCCP data (1991 to 1995), *Int. J. Climatol.*, *25*, 1103–1125, doi:10.1002/joc.1157.

Robock, A. (2013), The latest on volcanic eruptions and climate, *Eos Trans. AGU*, *94*(35), 305–306, doi:10.1002/2013EO350001.

Rolf, C., M. Krämer, C. Schiller, M. Hildebrandt, and M. Riese (2012), Lidar observation and model simulation of a volcanic-ash-induced cirrus cloud during the Eyjafjallajökull eruption, *Atmos. Chem. Phys.*, *12*, 10,281–10,294, doi:10.5194/acp-12-10281-2012.

Sassen, K. (1992), Evidence for liquid-phase cirrus cloud formation from volcanic aerosols: Climatic implications, *Science*, *237*(5069), 516–519, doi:10.1126/science.257.5069.516.

Sassen, K. (2002), Cirrus clouds: A modern perspective, in *Cirrus*, edited by D. Lynch et al., pp. 11–40, Oxford Univ. Press, New York.

Sassen, K., and S. Benson (2001), A midlatitude cirrus cloud climatology from the facility for atmospheric remote sensing. Part II: Microphysical properties derived from lidar depolarization, *J. Atmos. Sci.*, *58*, 2103–2112, doi:10.1175/1520-0469(2001)058<2103:AMCCCF>2.0.CO;2.

Sassen, K., D. Starr, G. G. Mace, M. R. Poellot, S. H. Melfi, W. L. Eberhard, J. D. Spinhirne, E. W. Eloranta, D. E. Hagen, and J. Hallett (1995), The 5–6 December 1991 FIRE IFO II jet stream cirrus case study: Possible influences of volcanic aerosols, *J. Atmos. Sci.*, *52*, 97–123, doi:10.1175/1520-0469(1995)052<0097:TDFIIJ>2.0.CO;2.

Sassen, K., Z. Wang, and D. Liu (2008), Global distribution of cirrus clouds from CloudSat/Cloud-Aerosol Lidar and Infrared Pathfinder Satellite Observations (CALIPSO) measurements, *J. Geophys. Res.*, *113*, D00A12, doi:10.1029/2008JD009972.

Sawamura, P., et al. (2012), Stratospheric AOD after the 2011 eruption of Nabro volcano measured by lidars over the Northern Hemisphere, *Environ. Res. Lett.*, *7*, 034013, doi:10.1088/1748-9326/7/3/034013.

Sheng, J.-X., D. K. Weisenstein, B.-P. Luo, E. Rozanov, A. Stenke, J. Anet, H. Bingemer, and T. Peter (2015), Global atmospheric sulfur budget under volcanically quiescent conditions: Aerosol-chemistry-climate model predictions and validation, *J. Geophys. Res. Atmos.*, *120*, 256–276, doi:10.1002/2014JD021985.

Song, N., D. O'C. Starr, D. J. Wuebbles, A. Williams, and S. M. Larson (1996), Volcanic aerosols and interannual variation of high clouds, *Geophys. Res. Lett.*, *23*, 2657–2660, doi:10.1029/96GL02372.

Stubenrauch, C. J., et al. (2013), Assessment of global cloud datasets from satellites: Project and database initiated by the GEWEX radiation panel, *Bull. Am. Meteorol. Soc.*, *94*, 1031–1049, doi:10.1175/BAMS-D-12-00117.1.

Theys, N., et al. (2013), Volcanic SO_2 fluxes derived from satellite data: A survey using OMI, GOME-2, IASI and MODIS, *Atmos. Chem. Phys.*, *13*, 5945–5968, doi:10.5194/acp-13-5945-2013.

Thomason, L. W., and J.-P. Vernier (2013), Improved SAGE II cloud/aerosol categorization and observations of the Asian tropopause aerosol layer: 1989–2005, *Atmos. Chem. Phys.*, *13*, 4605–4616, doi:10.5194/acp-13-4605-2013.

Vaughan, M. A., et al. (2009), Fully automated detection of cloud and aerosol layers in the CALIPSO lidar measurements, *J. Atmos. Oceanic Technol.*, *26*, 2034–2050, doi:10.1175/2009JTECHA1228.1.

Vernier, J.-P., et al. (2013), Comment on "Large volcanic aerosol load in the stratosphere linked to Asian monsoon transport", *Science*, *339*(6120), 647, doi:10.1126/science.1227817.

Wang, J., S. Park, J. Zeng, C. Ge, K. Yang, S. Carn, N. Krotkov, and A. H. Omar (2013), Modeling of 2008 Kasatochi volcanic sulfate direct radiative forcing: Assimilation of OMI SO2 plume height data and comparison with MODIS and CALIOP observations, *Atmos. Chem. Phys.*, *13*, 1895–1912, doi:10.5194/acp-13-1895-2013.

Wang, P.-H., P. Minnis, and G. K. Yue (1995), Extinction coefficient (1 μm) properties of high-altitude clouds from solar occultation measurements (1985–1990): Evidence of volcanic aerosol effect, *J. Geophys. Res.*, *100*, 3181–3199.

Wiacek, A., T. Peter, and U. Lohmann (2010), The potential influence of Asian and African mineral dust on ice, mixed-phase and liquid water clouds, *Atmos. Chem. Phys.*, *10*, 8649–8667, doi:10.5194/acp-10-8649-2010.

Wiesner, M. G., A. Wetzel, S. G. Catane, E. L. Listanco, and H. T. Mirabueno (2003), Grain size, areal thickness distribution and controls on sedimentation of the 1991 Mount Pinatubo tephra layer in the South China Sea, *Bull. Volcanol.*, *66*, 226–242, doi:10.1007/s00445-003-0306-x.

Winker, D. M., W. H. Hunt, and M. J. McGill (2007), Initial performance assessment of CALIOP, *Geophys. Res. Lett.*, *34*, L19803, doi:10.1029/2007GL030135.

Winker D. M., M. A. Vaughan, A. Omar, Y. Hu, K. A. Powell, Z. Liu, W. H. Hunt, and S. A. Young (2009), Overview of the CALIPSO Mission and CALIOP data processing algorithms, *J. Atmos. Oceanic Technol.*, *26*, 2310–2323, doi:10.1175/2009JTECHA1281.1.

Zhang, K., et al. (2012), The global aerosol-climate model ECHAM-HAM, version 2: Sensitivity to improvements in process representations, *Atmos. Chem. Phys.*, *12*, 8911–8949, doi:10.5194/acp-12-8911-2012.